Boosting Glioblastoma Therapy with Targeted Pyroptosis Induction

Fang, Xinggang; Chen, Zhuo; Zhou, Wenhui; Li, Tongfei; Wang, Man; Gao, Yujiu; Ma, Shinan; Feng, Ying; Du, Shiming; Lan, Peimin; Chen, Hanyu; Wei, Jiarui; Zhang, Sisi; Li, Zixiang; Liu, Xinglin; Zhang, Hongbo; Guo, Xingrong; Luo, Jie

Published in:
Small

DOI:
10.1002/smll.202207604

Published: 01/07/2023

Document Version
Final published version

NANO · MICRO small
www.small-journal.com

Boosting Glioblastoma Therapy with Targeted Pyroptosis Induction

Xinggang Fang, Zhuo Chen, Wenhui Zhou, Tongfei Li, Man Wang, Yujiu Gao, Shinan Ma, Ying Feng, Shiming Du, Peimin Lan, Hanyu Chen, Jiarui Wei, Sisi Zhang, Zixiang Li, Xinglin Liu, Hongbo Zhang, Xingrong Guo,* and Jie Luo**

Glioblastoma (GBM) is a highly aggressive cancer that currently lacks effective treatments. Pyroptosis has emerged as a promising therapeutic approach for cancer, but there is still a need for new pyroptosis boosters to target cancer cells. In this study, it is reported that Aloe-emodin (AE), a natural compound derived from plants, can inhibit GBM cells by inducing pyroptosis, making it a potential booster for pyroptosis-mediated GBM therapy. However, administering AE is challenging due to the blood-brain barrier (BBB) and its non-selectivity. To overcome this obstacle, AE@ZIF-8 NPs are developed, a biomineralized nanocarrier that releases AE in response to the tumor's acidic microenvironment (TAM). Further modification of the nanocarrier with transferrin (Tf) and polyethylene glycol-poly (lactic-co-glycolic acid) (PEG-PLGA) improves its penetration through the BBB and tumor targeting, respectively. The results show that AE-NPs (Tf-PEG-PLGA modified AE@ZIF-8 NPs) significantly increase the intracranial distribution and tumor tissue accumulation, enhancing GBM pyroptosis. Additionally, AE-NPs activate antitumor immunity and reduce AE-related toxicity. Overall, this study provides a new approach for GBM therapy and offers a nanocarrier that is capable of penetrating the BBB, targeting tumors, and attenuating toxicity.

1. Introduction

As a grade IV glioma, glioblastoma (GBM) is the most common and deadly intracranial malignant tumor which has high mortality and morbidity rates and a low effective cure rate.[1,2,3] Surgical therapy is the preferred treatment, but the complete recession is difficult and resulting in a high recurrence rate especially in invasive growth GBM cases.[4] In addition, the creative structure of the blood–brain barrier (BBB) fairly restricted the using of traditional chemotherapies for GBM therapy.[5] And the suppressed immune microenvironment also worsens the prognosis of GBM.[6] Thus, new therapies for GBM are still highly demanded.

Pyroptosis, which is a programmed cell death depending on the activation of gasdermin family (GSDMs), the activation of which further induces cell

X. Fang, Z. Chen, J. Luo
Clinical College of Traditional Chinese Medicine
Taihe Hospital
Hubei University of Chinese Medicine
Wuhan, Hubei 430065, P. R. China
E-mail: yueli@taihehosptial.com

X. Fang, Z. Chen, Y. Gao, S. Ma, Y. Feng, S. Du, S. Zhang, Z. Li, X. Guo, J. Luo
Department of Neurosurgery
Hubei Key Laboratory of Embryonic Stem Cell Research
Hubei Clinical Research Center for Umbilical Cord Blood Hematopoietic Stem Cells
Taihe Hospital
Hubei University of Medicine
Shiyan, Hubei 442000, P. R. China
E-mail: gxrdl@hbmu.edu.cn

X. Fang, P. Lan, H. Chen
Department of Integrated Chinese and Western Medicine
Taihe Hospital
Hubei University of Medicine
Shiyan, Hubei 442000, P. R. China

The ORCID identification number(s) for the author(s) of this article can be found under https://doi.org/10.1002/smll.202207604.

DOI: 10.1002/smll.202207604

W. Zhou, H. Zhang
Pharmaceutical Sciences Laboratory
Åbo Akademi University
20520 Turku, Finland
E-mail: hongbo.zhang@abo.fi

W. Zhou, H. Zhang
Turku Bioscience Centre
University of Turku and Åbo Akademi University
20520 Turku, Finland

T. Li, J. Wei
School of Basic Medical Sciences
Hubei University of Medicine
Shiyan, Hubei 442000, P. R. China

M. Wang
Pharmacy intravenous admixture service
Taihe Hospital
Hubei University of Medicine
Shiyan, Hubei 442000, P. R. China

X. Liu
Institute of Biomedicine
Hubei University of Medicine
Shiyan, Hubei 442000, P. R. China

membrane pore-forming and GSDMs N-terminal fragment release, causing intracellular and extracellular osmotic pressure imbalance, cell swelling and rupture, and then leakage of cytoplasmic pro-inflammatory cytokines, resulting in cell death.[7,8] More importantly, depend on membrane ruptures and cellular contents release, cytotoxic lymphocytes were activated to kill tumor cells, which was closely involved in anticancer immune response and rising as a very promising method for cancer treatment.[9] As an important pyroptosis pathway, activation of caspase-3/gasdermin E (CASP3/GSDME) can further trigger the activation of host immune system,[10] which stimulates a "cold" tumor microenvironment to be an immunogenic "hot" tumor microenvironment,[8] and showed significant inhibitory effects on multiple tumors, such as breast cancer, melanoma, gastric cancer, lung cancer, hepatocellular carcinoma, etc.[11,12] And lots of effort have been done to utilize the pyroptosis pathway as target for cancer therapy. For example, many chemotherapeutic drugs, such as doxorubicin and cisplatin have been shown to have the potential to induce pyroptosis. However, the drug-related side effects and drug resistance are still the main problems. Therefore, the finding of new novel pyroptosis activator still has a promising contribution for GBM immunotherapy.

Aloe-emodin (AE), an anthraquinone derivative extracted from a variety of natural plants has aroused increased attention for cancer therapy during recent years because of its wide range of pharmacological effects, which include antiviral, antibacterial, antiallergic, antiosteoporosis, antidiabetic, neuroprotective, and antitumors by induction of DNA damage, cell cycle arrest, and inhibit cell migration.[13,14] In this work, we found that AE suppressed GBM cells in a time- and concentration-dependent manner, and the mechanism studies investigated that this antitumor effect may arise from the activation of the CASP3/GSDME pyroptosis pathway. Thus, AE may act as a pyroptosis booster for GBM therapy. Moreover, our analyzing results from the Cancer Genome Atlas (TCGA) database showed that GSDME, which is a key modulator for pyroptosis is highly expressed in GBM relative to adjacent tissues (Figure 2F,G). Therefore, targeting GSDME by AE might serve as a good strategy for GBM treatment via immunotherapy.

However, similar to other fat soluble drugs, poor water solubility, as well as BBB penetration, and nonselection remain the main obstacles to applying AE in GBM treatment. In recent years, multiple strategies have been reported to improve BBB penetration or tumor targeting, such as polymeric nanoparticles, nanoemulsions, liposomes, micelles, and exosomes,[15] such strategies partially improved BBB penetration or tumor targeting. But as an intracranial tumor, GBM treatment faces the dual challenges of BBB and tumor targeting. Notably, GSDME is also expressed in normal brain, and nonselective activation of GSDME have the risk of normal brain injury, thus an ideal drug delivery carrier for intracranial tumors needs to have both BBB penetration, tumor targeting, and tumor acid microenvironment (TAM) controlled release ability. To meet the requirements, we first biomineralized AE with zeolitic imidazolate framework nanoparticles (ZIF-8 NPs), which are zinc ions and dimethylimidazole composed metal–organic framework (MOF) based NPs and have been widely used for biomolecular intracellular delivery owing to their easy preparation, good biocompatibility, and acidic microenvironments responsive degradation.[16] Therefore, ZIF-8 NPs may sever as a good method for improving the solubility and tumor targeting of AE. Moreover, since Zn^{2+} is a positive regulator for both innate immunity and adaptive immunity,[17] we supposed that the released Zn^{2+} during ZIF-8 NPs degradation in GBM cancer cells is also a good factor for improving the suppressed immune microenvironment. Thereby, the immune response induced by pyroptosis of GBM cells will be enhanced.

It was reported that Poly (lactic-*co*-glycolic acid) (PLGA) polymer is with good biocompatibility, biodegradability, and no toxicity,[18] thus is widely used to improve BBB permeability both in vitro and in vivo, however, they are readily cleared by the reticuloendothelial system (RES) through protease-mediated phagocytosis.[19] But the remarkable thing is that PLGA modified with polyethylene glycol (PEG) prolongs circulation time in vivo and improves water solubility and stability.[20,21] Therefore, to increase the blood circulation time, BBB penetration ability, as well as minimize the none-selected cytoxicity of AE loaded ZIF-8 NPs (AE@ZIF-8 NPs), we further coated AE@ZIF-8 NPs with transferrin (Tf) modified PEG-PLGA polymer (Tf-PEG-PLGA). Tf is a ligand of Tf receptor (TfR),which is highly expressed in the endothelium of brain capillaries and tumor tissue.[22,23] Thus, by targeting the TfR of brain capillaries endothelium cells and tumor cells, we expect that the AE-NPs will first across the BBB and enter the brain in an efficient active transport mode,[23] and then realizing the enrichment in GBM tumor cells. On the whole, ZIF-8 NPs can provide a good solution for in vivo administration of AE and also act as a immuno response regulator, and Tf-PEG-PLGA polymer coating enable the AE-NPs across the BBB and finally accumulating in the GBM tumor cells.

Our data demonstrated that, AE induced GBM tumor cells death in a time and concentration dependent manner by activation of CASP3/GSDME pyroptosis pathway. By loading AE in ZIF-8 NPs, TAM targeted AE release was realized. And the Tf-PEG-PLGA polymer coating significantly increased the intracranial distribution and tumor enrichment, therefore, boosted pyroptosis in the tumor cells and enhanced antitumor effects of AE@ZIF-8 NPs. Furthermore, AE-NPs also enhanced microglia GBM infiltration and M1 subtype polarization, increased CD8+ T cell expression, prolonged the survival rate of tumor-bearing mice, and reduced AE-related hepatotoxicity and nephrotoxicity. In summary, our work offers a new strategies for GBM targeted therapy, and the newly constructed AE loaded Tf-PEG-PLGA coated ZIF-8 nanoparticles(AE@ZIF-8/Tf-PEG-PLGA NPs, AE-NPs) can be served as an effective, safe, and BBB penetrative pyroptosis booster for intracranial tumor therapy.

2. Results

2.1. AE Inhibited Proliferation and Induced Pyroptosis in GBM Cells

Previous studies have shown that AE is a natural monomeric compound with antitumor effects (**Figure 1**A).[24] However,

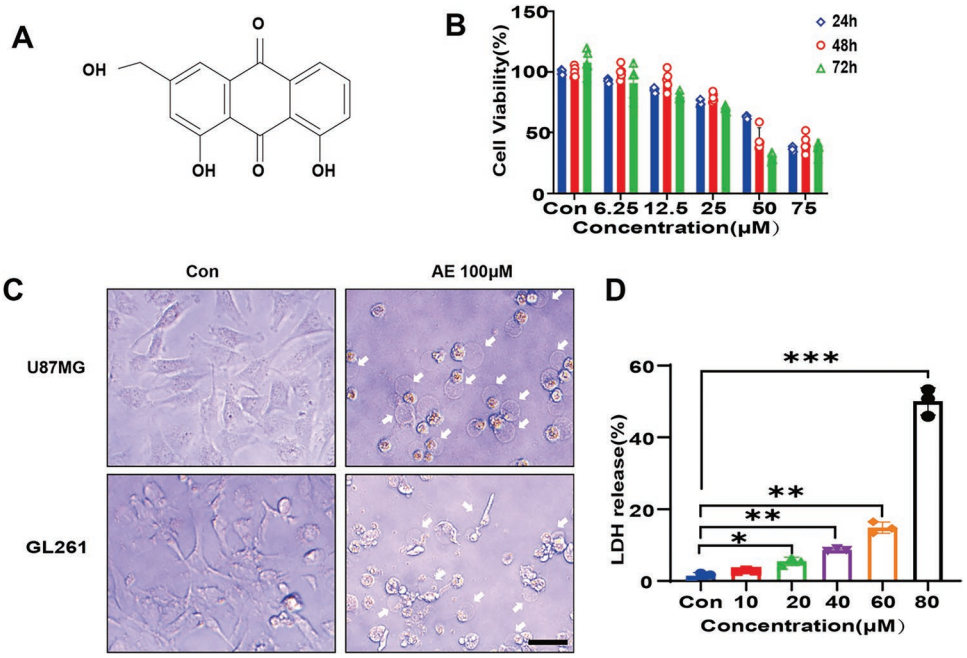

Figure 1. AE induced pyroptosis in GBM cells. A) Chemical structure of AE. B) Cell viability was tested by CCK-8 in AE-treated GL261 cells. All values are presented as mean ± SD ($n = 4$). C) Representative photographs of U87MG and GL261 cells treated with AE for 60 h. The white arrows indicate pyroptotic cells (scale bar: 200 μm). D) LDH release of U87MG cells treated with AE for 60 h. Data are presented as mean ± SD ($n = 3$); $^{*}P < 0.05$, $^{**}P < 0.01$, $^{***}P < 0.001$(one-way ANOVA and Bonferroni's multiple comparisons test).

its role in antiglioma is currently not very clear. To explore the potential anti-GBM activity, we administered AE to GBM human cell line U87MG and GBM mouse cell line GL261. Cell Counting Kit 8 (CCK-8) assay showed that AE suppressed GBM cells in a time- and concentration-dependent manner (Figure 1B; and Figure S1, Supporting Information), and the morphology of AE-treated GBM cells showed pyroptosis-specific features, such as cell membrane swelling and blebbing (Figure 1C), suggesting that AE may induced GBM cells pyroptosis. Because pyroptosis is accompanied with lactate dehydrogenase (LDH) extracellular release,[25] to further confirm AE-induced pyroptosis, we next measured LDH release from AE treated U87MG cells, and showed that LDH release was increased with the increasing of AE concentration (Figure 1D). These results indicated that, AE inhibited cell proliferation and induced pyroptosis in GBM cells.

2.2. AE Activated the CASP3/GSDME Pyroptosis Pathway in GBM Cells

Pyroptosis is mainly activated through the caspase-1/gasdermin D (CASP1/GSDMD) pathway or CASP3/GSDME pathway.[26] To clarify the mechanism of AE-mediated pyroptosis, AE-GBM network pharmacology analysis was performed. A Venn diagram with the overlapping targets related to AE and GBM identified 44 promising targets for GBM treatment of AE (**Figure 2**A). The network of these 44 targets was analyzed with the STRING database (Figure 2B), and the PPI network showed 44 nodes and 473 edges. We next analyzed each node and screened out the first 20 targets with node degrees greater than 23. These targets included AKT1, ALOX5, AKT2, BCL2L1, CASP3, CASP9, CDK2, and CDK6. Among them, CASP3 is one of the core intersection targets (Figure 2C). Since CASP3 is the key protein of CASP3/GSDME pyroptosis pathway, we speculated that AE may induce GBM pyroptosis through the CASP3/GSDME pathway. And this was confirmed by in vitro studies with AE inducing CASP3 and GSDME activation but not GSDMD (Figure 2D,E), which is similar to cisplatin, a classic pyroptosis-inducer, and this activation can be inhibited by z-VAD-FMK (Figure S2, Supporting Information). Furthermore, we found that AE increasing the expression of GSDME at mRNA (Figure S3, Supporting Information) and protein levels (Figure S4, Supporting Information).

A previous report showed that GSDME expression determines whether pyroptosis is dominant in the antitumor process induced by chemotherapeutic drugs.[27] We next analyzed the expression of GSDME in GBM cell lines and tumor tissues by western blot (WB) and TCGA database. The analyzing result from the TCGA database (http://ualcan.path.uab.edu/index.html) showed that, compared to other tumors and normal brain tissue, GSDME was higher expressed in GBM (Figure 2F,G). And the WB showed that GSDME was negatively expressed in HMO6 (human microglia cell line) cells, and higher expressed in human GBM cell lines U87MG, DBTRG, and then HepG2, Hela, A549, even in mouse cells. Most importantly, GSDME is higher expressed GBM cell line GL261 then microglia cell line BV2 (Figure 2H). These results suggesting that GSDME is a good target for anti-GBM therapy by activating of the CASP3/GSDME pyroptosis pathway.

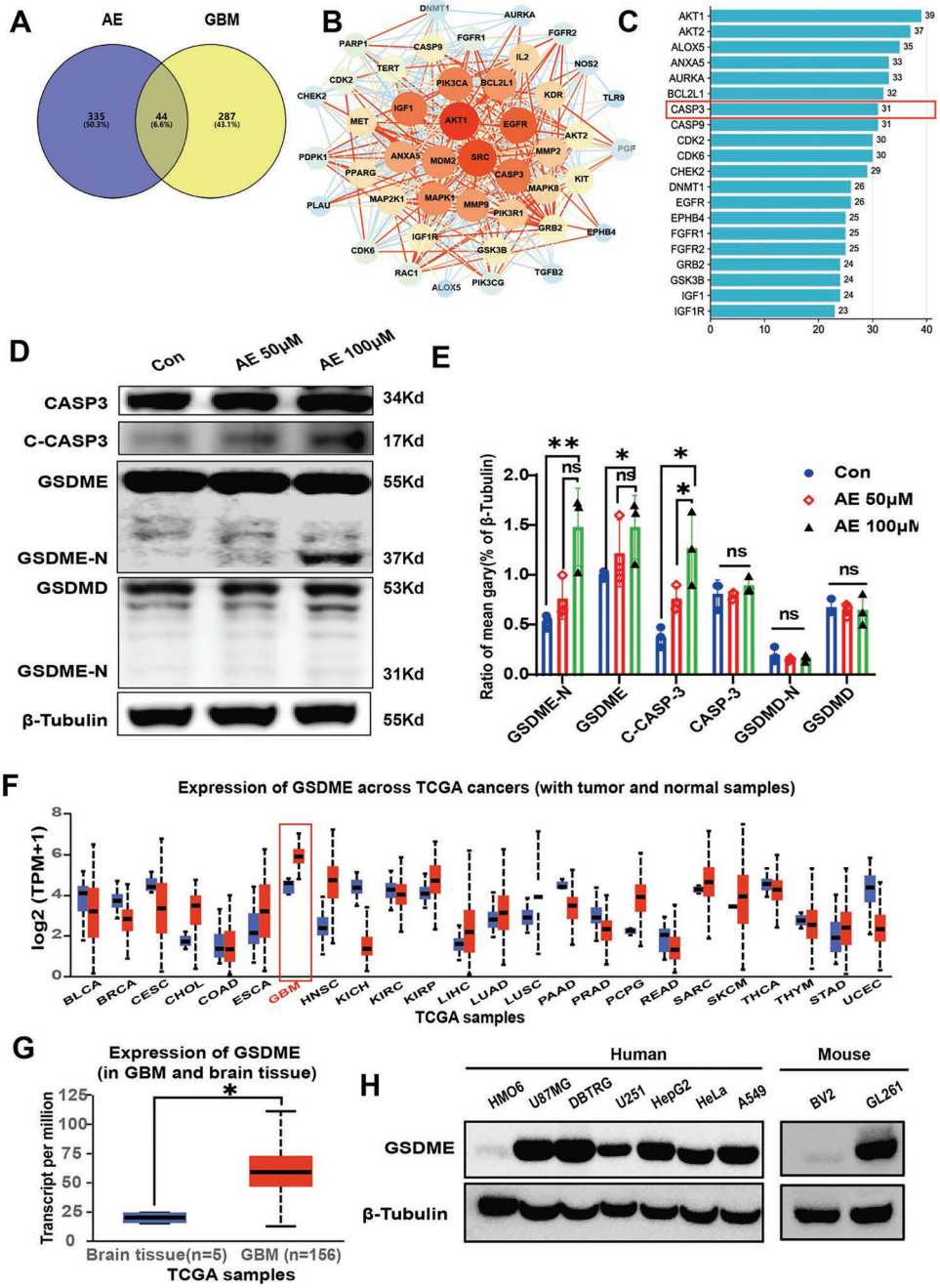

Figure 2. AE activated the CASP3/GSDME pyroptosis pathway in GBM cells. A) 44 intersection targets of AE and GBM illustrated by Venn diagram. B) Cytoscape-based PPI analysis construction (intensity of the node color is proportional to the amounts of linked proteins). C) Bar plot of the top 20 targets in the PPI network. CASP3 is one of the core intersection targets. D) The expression of CASP3, cleaved caspase-3(C-CASP3), GSDME, and GSDME-N terminal (GSDME-N), GSDMD, GSDMD-N terminal (GSDMD-N), biomarkers of pyroptosis, was assayed by WB. E) Quantitatively analyzed CASP3, C-CASP3, GSDME, GSDME-N, GSDMD, GSDMD-N by the mean gray value. All the data are presented as the mean ± SD from three independent experiments ($n = 3$); * $P < 0.05$, (one-way ANOVA and Bonferroni's multiple comparisons test). F) Expression of GSDME across TCGA cancers from TCGA database. G) Expression of GSDME in GBM and brain tissue from TCGA database (*$P < 0.05$). H) Expression of GSDME in different tumor cell lines and normal cell lines, tested by western blot.

2.3. Characterization and Acidic Microenvironment Responsiveness of AE-NPs

Previous studies have shown that lack of selectivity distribution and poor water solubility in vivo can lead to low efficacy and off-target side effects.[28,29] To improve the intracranial distribution and tumor enrichment of AE, AE-NPs were constructed by a two-step method (**Scheme 1**A). First, AE@ZIF-8 nanoparticles were synthesized by encapsulating AE during the mineralization of zinc nitrate and 2-methylimidazole. Sub-

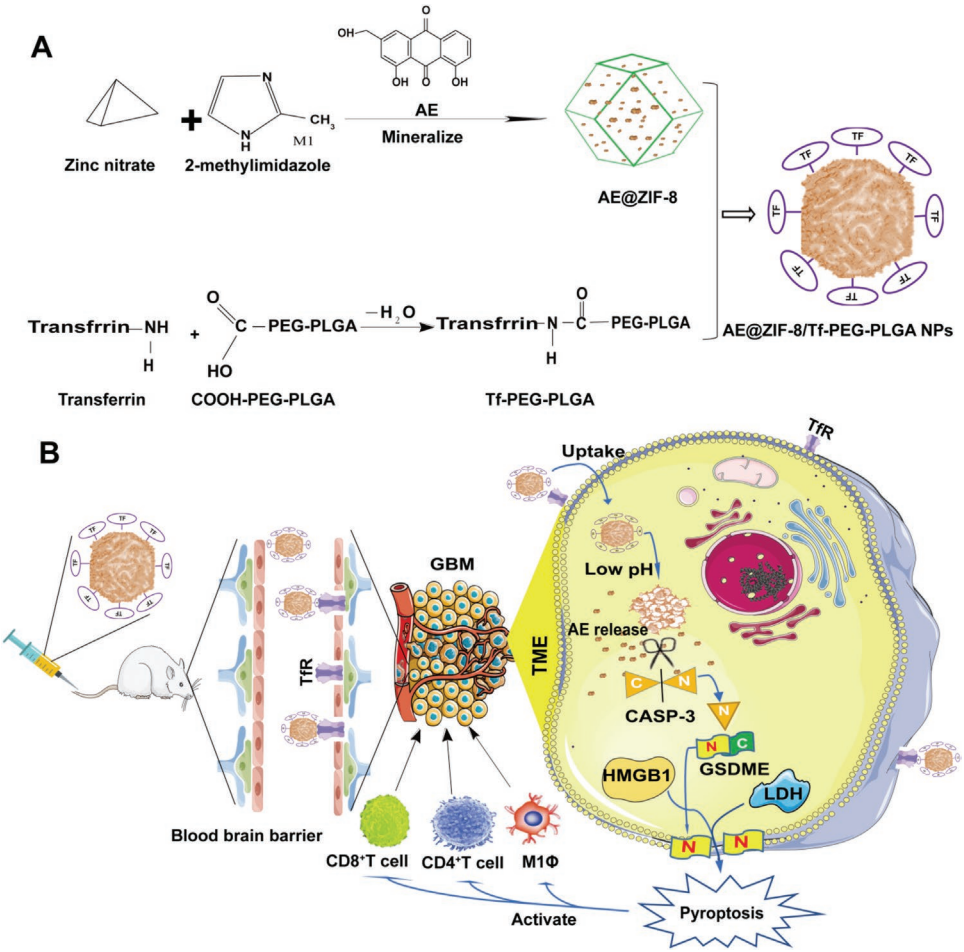

Scheme 1. Preparation (A), in vivo delivery, and anti-GBM mechanism (B) schematic diagram of AE@ZIF-8/Tf-PEG-PLGA NPs (AE-NPs).

sequently, AE@ZIF-8 NPs were coated with Tf-PEG-PLGA polymer. The appearances of blank ZIF-8, AE@ZIF-8, and AE-NPs were shown in **Figure 3**A. During the formation of AE@ZIF-8, increasing AE dosage increased the particle size, and UV-absorption peak (255 nm) (Figure S5A,C, Supporting Information), while the average ζ potential was decreased (Figure S5B, Supporting Information). However, a stable UV-absorption curve could not be formed with AE concentrations of 20 mg (Figure S5C, Supporting Information). Therefore, 10 mg AE was selected for the final AE@ZIF-8 NPs formulation and subsequent experiments. The AE loading degree was 43.2%, AE encapsulation rate of AE@ZIF-8 is 32.6%, and the hydrodynamic size of AE@ZIF-8 measured by dynamic light scattering (DLS) was 155.1 ± 42.41 nm (Figure 3B), while the size measured by transmission electron microscopy (TEM) was 38.87 ± 4.71 nm (Figure S8, Supporting Information), and the surface zeta potential was 20.3 ± 7.95 mV (Figure 3C) in methanol. Next, AE-NPs were prepared according to an established protocol, while the increased ratio of AE@ZIF-8 NPs to Tf-PEG-PLGA polymer decreased the particle size (Figure S6A, Supporting Information), but the surface zeta potential, UV–vis absorption and AE loading degree were increased (Figure S6B–D, Supporting Information). The transferrin conjunction degree decreased significantly when the dosage ratio was higher than 7:3 (Figure S6E, Supporting Information), thus a volume ratio of 7:3 was chosen for final AE-NPs preparation and subsequent experiments. Then hydrodynamic size of AE-NPs measured by DLS was 199 ± 85 nm (Figure 3B), and remains stable for 96 h (Figure 3G), while the size measured in the TEM image was 46.52 ± 6.43 nm (Figure S8, Supporting Information), the surface zeta potential was 13.8 ± 6.49 nm (Figure 3C), the AE loading rate was 15.43% (Figure S6D, Supporting Information), AE encapsulation rate of AE-NPs is 22.5%. Because the normal brain interstitial space is 38–68 nm,[30] and the tumor tissue intercellular space is 7–100 nm,[31] these suggests that our prepared AE-NPs can freely pass through the brain interstitial and tumor cell space. In addition, characterization data were expanded in biological solutions of normal saline containing 1% F127 (1% F127 NS) and 1% F127 NS with 10% FBS (1% F127 NS+10% FBS), in biological solutions, particles size are increased and zeta potential were decreased (Figure S7A–C, Supporting Information). This may be protein in biological solutions adsorbed on the nanoparticles' surface changed the characterization.

When blank ZIF-8 NPs, AE@ZIF-8 NPs, and AE-NPs were detected by TEM, the surface of AE-NPs had a prominent Tf-PEG-PLGA coating (amaranth arrows in Figure 3E). The Fourier transform infrared (FTIR) spectrum of AE-NPs also revealed new absorption peaks between 1500 and 1700 cm^{-1}

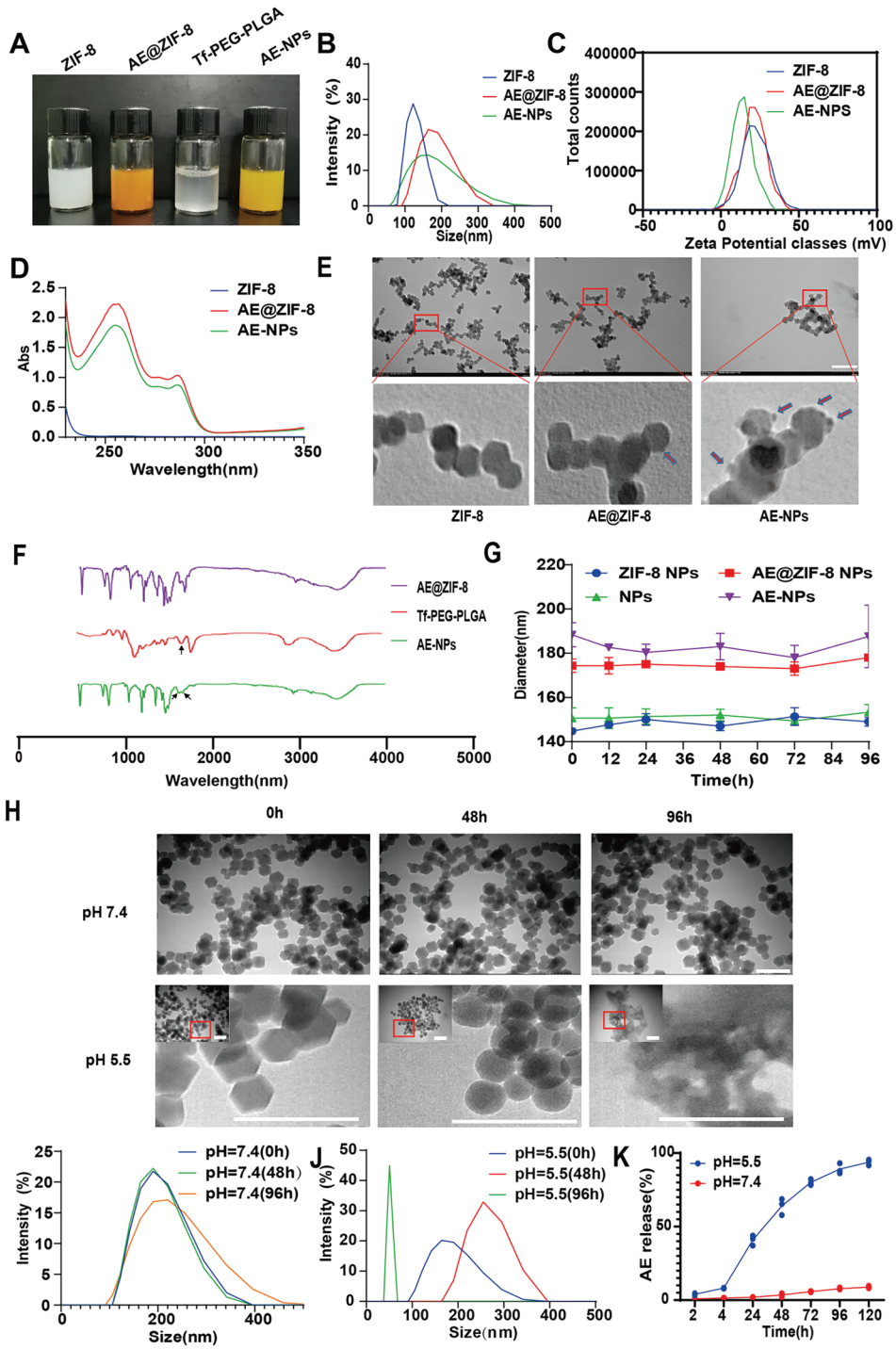

Figure 3. Characterizations and acid-microenvironmental response of AE-NPs. A) Appearance. B) Size results from DLS. C) Zeta potential. D) UV–vis absorption spectra. E) TEM images (scale bar: 200 nm). F) FTIR spectra of AE@ZIF-8, TF-PEG-PLGA, and AE-NPs, arrow point to stretching vibration peak of —CO—NH— from the amide bonds of transferrin connect to PEG-PLGA and contained in Tf. G) Stability of different nanoparticles within 96 h. H) Morphology of AE-NPs in response to pH 7.4 and pH 5.5 for 48 and 96 h (Scale bar: 200 nm). I,J) Size of AE-NPs in pH 7.4 and pH 5.5 solutions at different time points. K) AE cumulative release profiles in 1% F127 NS, pH 7.4, and 5.5 from AE-NPs ($n = 3$).

compared with the spectrum of AE@ZIF-8 (Figure 3F). These may be resulted by the stretching vibration peak of —CO—NH— from the amide bonds of transferrin to PEG-PLGA, suggesting that AE-NPs were successfully prepared.

The acidic environment-responsive degradation ability makes ZIF-8 NPs are efficient carriers to target tumors and intracellular environment.[16,32] To test whether the Tf-PEG-PLGA polymer coating could interfere the pH responsive properties

of ZIF-8 NPs, we further performed pH degradation assay. Our experiments showed that the AE-NPs were stable in a neutral environment (pH = 7.4) but degraded with AE released in an acidic environment (pH = 5.5) (Figure 3H–K). These results suggest that AE-NPs react with the acidic microenvironment.

2.4. NPs Elevated Intracellular Uptake and AE-Mediated GBM Pyroptosis In Vitro

To evaluate the cellular uptake of AE-NPs by GBM cells, we encapsulated the fluorescent dye indocyanine green in ZIF-8 particle (ICG@ZIF-8) and Tf-PEG-PLGA polymer coated ZIF-8 NPs (ICG-NPs) (Figure S9, Supporting Information). Flow cytometry analysis showed that ICG, ICG@ZIF-8, and ICG-NPs (ICG concentration equilibrated to 3 μg mL^{-1}) entered U87MG cells in a time-dependent manner (**Figure 4**A). The proportion of ICG positive cells and their fluorescence intensity were significantly higher in ICG-NPs groups than ICG and ICG@ZIF-8 groups at each time point (Figure 4B). Therefore, we speculate that Tf-PEG-PLGA polymer coated ZIF-8 NPs increased intracellular uptake of ICG by U87MG cells. We next treated U87MG cells with ICG, ICG@ZIF-8, and ICG-NPs for 6 h (ICG concentration equilibrated to 3 μg mL^{-1}). Laser scanning confocal microscopy (LSCM) showed that the fluorescence intensity of the ICG-NPs groups was significantly enhanced in ICG-NPs treated groups (Figure 4C), confirming increased uptake.

Since Tf-PEG-PLGA polymer coated ZIF-8 NPs increased the intracellular uptake of cargo, we were wondering if the antitumor effect of AE was also enhanced by Tf-PEG-PLGA polymer coated ZIF-8 NPs. Therefore, we next treated U87 MG cells with AE and AE-NPs for 24 h and cell viability was measured. AE encapsulation with NPs exhibited a significantly higher inhibitory effect (Figure 4D). To investigate whether elevated cellular uptake impacts the cell death mechanism, we next observed AE and AE-NPs treated U87MG cells with a confocal high-intensity imaging analysis system. The results showed that pyroptosis occurred within 24 h in the AE-NPs treated group but took over 60 h in the AE group (Figure 4E), that was confirmed by the GSDME cleavage in AE-NPs group but not AE group in 24 h (Figure 4F). This suggests that the encapsulation of AE by Tf-PEG-PLGA polymer coated ZIF-8 NPs further increased the anti-GBM cells effect via enhanced pyroptosis.

2.5. AE-NPs Increased Intracranial Distribution and Tumor Enrichment of AE In Vivo

The main challenge for chemotherapeutic drugs in GBM treatment is BBB penetration and tumor targeting. Therefore, free ICG, ICG@ZIF-8, ICG-NPs were prepared as nanotracers to evaluate the biodistribution, BBB penetration, and tumor targeting capability of Tf-PEG-PLGA coated ZIF-8 NPs in vivo. As scheduled, C57BL/6J mice were first treated with ICG, ICG@ZIF-8, and ICG-NPs through the tail vein (ICG was normalized to 3 mg kg^{-1}), and then optical live imaging was performed to detect the biodistribution of ICG in brain and main organs at each time points. The results showed that compared with ICG and ICG@ZIF-8, ICG-NPs had a superior intracranial enrichment within 15 min and with obvious intracranial retention after 24 h (**Figure 5**A,B), liquid chromatography-mass spectrometry (LC-MS) quantification further confirmed there was a higher AE concentration in AE-NPs group in brain then other groups within 2 h (Figure 5D; and Figure S10, Supporting Information). Organ distribution showed that Tf-PEG-PLGA coated ZIF-8 NPs prolonged the retention time in the body. Our study also showed that, compared with free ICG, ICG@ZIF-8 exhibited lower brain distribution in early time, but had a longer detention time (Figure 5A–C). These findings indicated that loading with Tf-PEG-PLGA coated ZIF-8 NPs enhanced the ability of the cargo enter into the brain, and prolonged residence time. Subsequently, to evaluate tumor targeting ability, cryosections of tumor bearing brain from ICG and ICG-NPs treated mice were prepared. The results showed that ICG-NPs were remarkably enriched in tumor tissue (Figure 5E; and Figure S11, Supporting Information), LC-MS quantification further confirmed that the tumor tissue of AE-NPs group had higher AE concentration (Figure 5D; and Figure S10, Supporting Information). These findings suggested that Tf-PEG-PLGA coated ZIF-8 NPs enhanced intracranial distribution and tumor targeting.

2.6. AE-NPs Enhanced AE-Mediated Antitumor Effects In Vivo

To further evaluate the antitumor effect of AE-NPs, in vivo assay on GL261 orthotopic GBM mouse model was performed. Upon inoculation and tumor establishment, animals were randomly divided into four groups, and 1% F127 NS, AE, Tf-PEG-PLGA polymer coated ZIF-8 NPs (NPs), AE@ZIF-8 AE-NPs were administered through the tail vein every 2 days. Body weight, tumor luciferase expression, and mental status were measured weekly (**Figure 6**A). The results showed that after 1 week administration, the fluorescence of GBM in the control (Con) group, NPs group, and AE group increased continuously, especially in the Con group. In contrast, it was decreased in the AE-NPs group (Figure 6B,C). Compared with the other three groups, AE-NPs showed a stronger effect on tumor volume and weight reduction. Furthermore, compared to the control group, NPs also reduced tumor volume and weight (Figure 6D,E), which may be attributed to the cytotoxic effect of ZIF-8 NPs.[16,33] Although NPs and AE have similar effects on tumor volume and weight reduction, the AE group showed increased tumor necrosis in histopathology (Figure 6F).

Finally, hematoxylin and eosin staining (HE), Ki-67 staining and WB assays were performed to clarify mechanism of AE-NPs act on GBM. HE staining showed that tumor necrosis was happened in all groups, but more obvious in AE, AE@ZIF-8, and AE-NPs groups (Figure 6F). Ki-67 staining is a biomarker of proliferation, immunohistochemical results showed that AE-NPs treated GBM tissue displayed lower Ki-67 expression (Figure 6G,H), and supporting inhibited proliferation. At the end of the administration, the terminal survival rate was better in the AE-NPs group than in the other 4 groups (Figure 6I). Together these results suggest that AE-NPs promote necrosis, inhibit of GBM growth, and ameliorated the prognosis. Subsequently, to further confirm the antitumor mechanism at

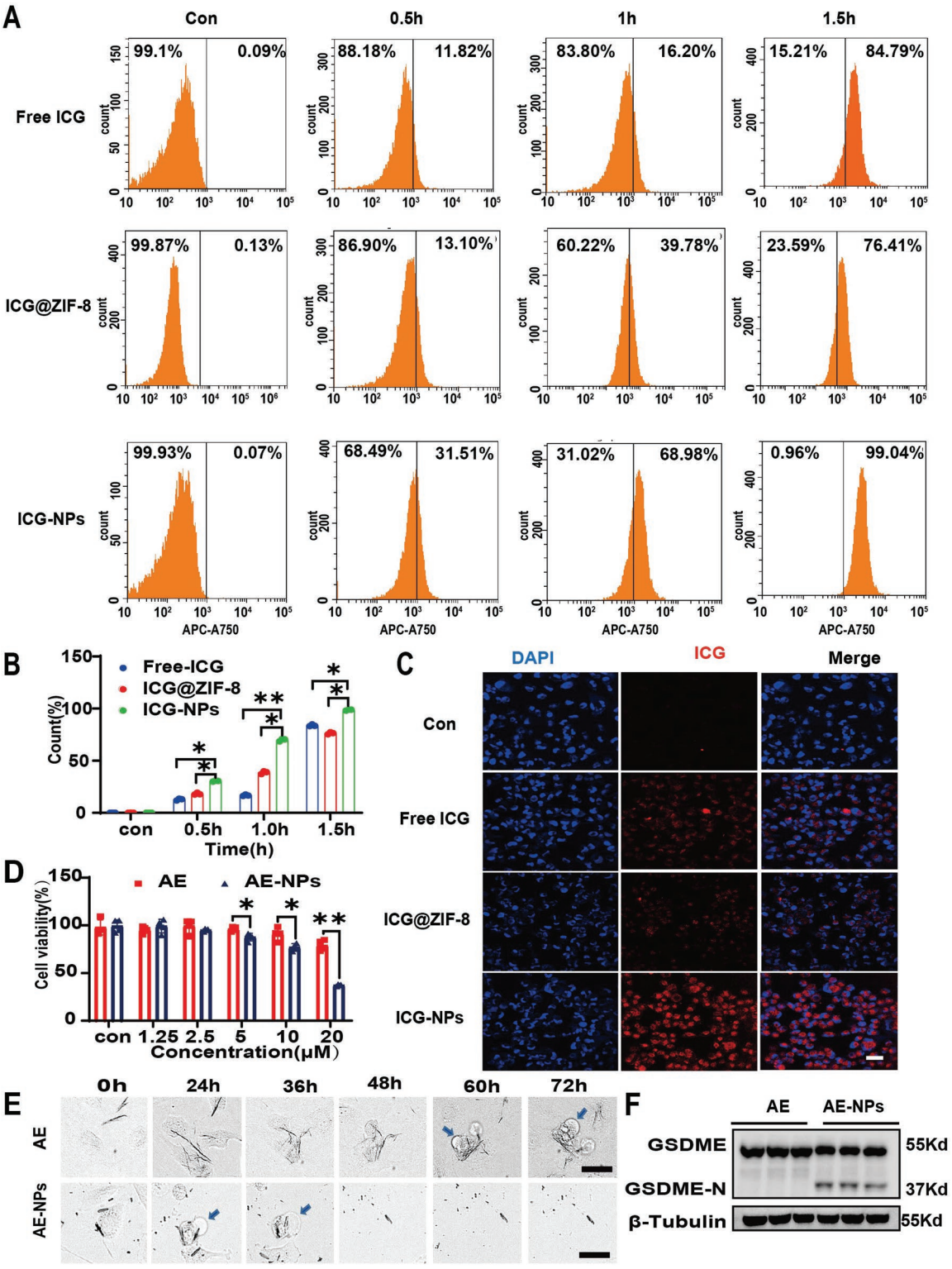

Figure 4. AE-NPs enhanced intracellular uptake and AE-mediated GBM cell pyroptosis in vitro. A,B) ICG, ICG@ZIF-8, and ICG-NPs intracellular uptake by U87MG for 0.5, 1, and 1.5 h, ICG was normalized to 3 μg mL^{-1} assessed by flow cytometry, Data are presented as the mean ± SD from three independent experiments; * $P < 0.05$, ** $P < 0.01$ (one-way ANOVA and Bonferroni's multiple comparisons test) ($n = 3$). C) Confocal microscopy images of ICG, ICG@ZIF-8, and ICG-NPs (ICG was normalized to 3 μg mL^{-1}) intracellular uptake by U87MG cells for 6 h (scale bar: 200 μm). D) Cytotoxicity on U87MG of AE and AE-NPs for 24 h, test by CCK-8. All data are presented as the mean ± SD ($n = 3$), *$P < 0.05$, **$P < 0.01$ (two-tailed *t*-test). E) Confocal high-intensity imaging of U87MG cells treated with AE and AE-NPs (AE was normalized to 20 μM) at different time points. Green arrows indicate pyroptotic cells (scale bar: 200 μm). F) Expression of GSDME-N terminal in U87MG cells after AE and AE-NPs treated for 24 h (AE was normalized to 20 μM), tested by WB.

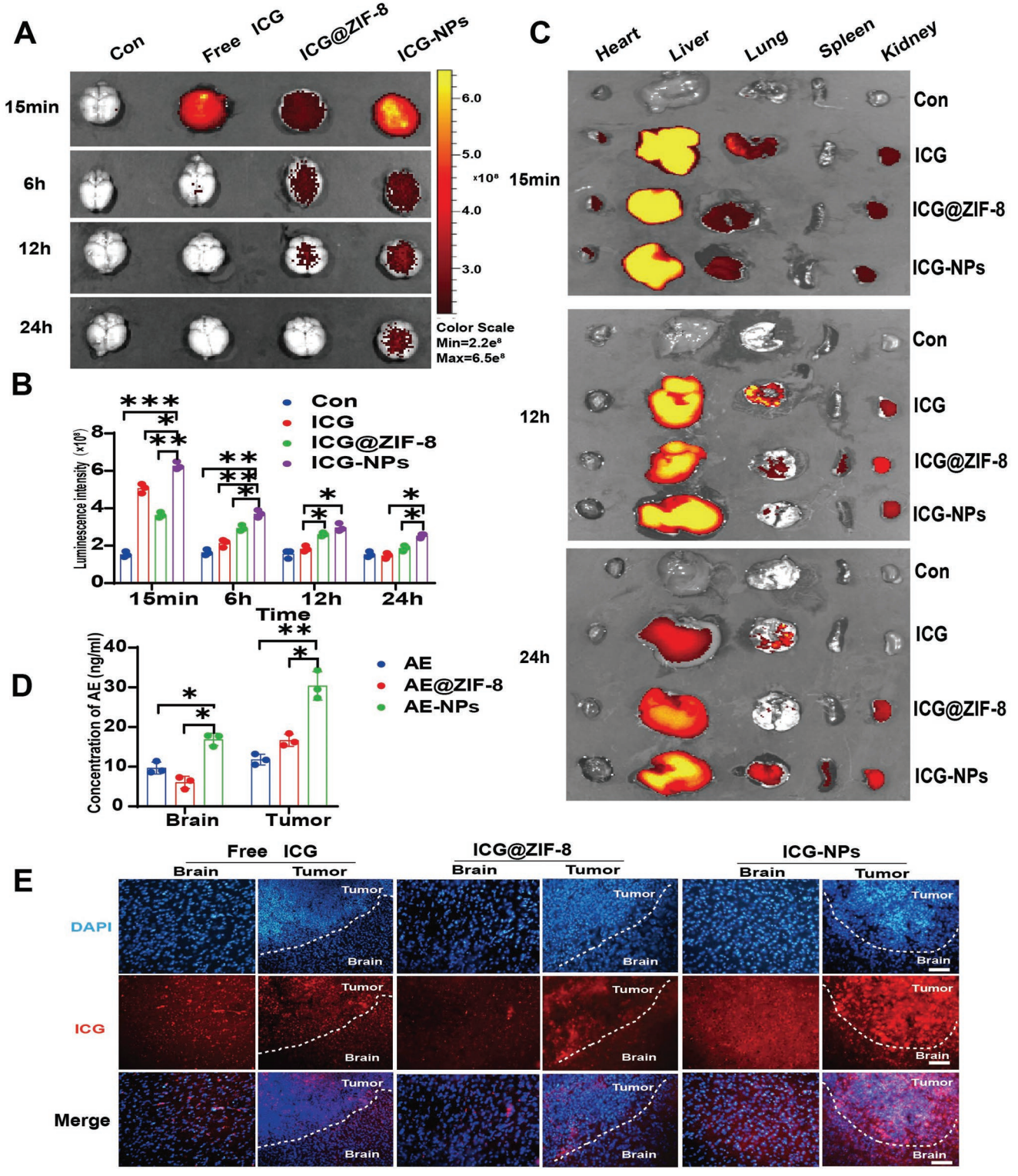

Figure 5. AE-NPs improved the intracranial distribution and tumor enrichment in vivo. Optical live imaging detection (A) and quantification (B) of the intracranial distribution of ICG from ICG, ICG@ZIF-8, and ICG-NPs treated mice for 15 min, 6 h, and 12 h. ICG was normalized to 3 mg kg^{-1}. Data are presented as the mean ± SD from three independent experiments. *$P < 0.05$, **$P < 0.01$, ***$P < 0.001$ (one-way ANOVA and Bonferroni's multiple comparisons test). C) Organ distribution of ICG from ICG ICG@ZIF-8 and ICG-NP treated mice in different time point. D) Quantitation of AE concentration in brain and tumors from tumor bearing mice of different treatment by LC-MS. AE was normalized to 8 mg kg^{-1}, Data are presented as the mean ± SD from three independent experiments; *$P < 0.05$, **$P < 0.01$ (one-way ANOVA and Bonferroni's multiple comparisons test). E) Brain distribution of ICG (red) from ICG, ICG@ZIF-8, and ICG-NP-treated GBM bearing mice for 6 h. ICG was normalized to 3 mg kg^{-1} and assayed by cryosection with confocal microscopy (scale bar: 200 µm).

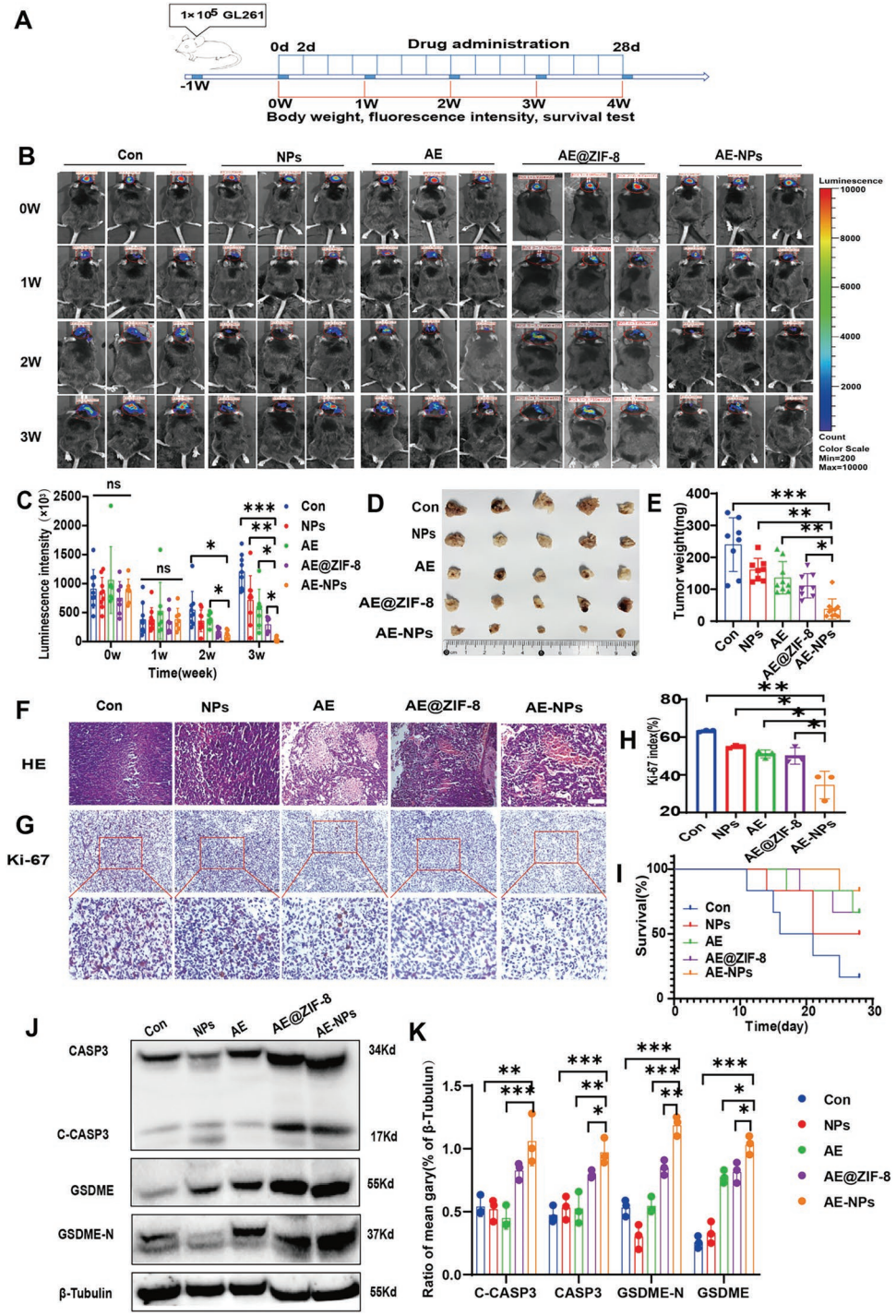

Figure 6. NPs enhanced the antitumor effects of AE in vivo. A) Administrative protocol in vivo. B) Fluorescent staining of GL261 tumor-bearing mice treated with 1% F127 NS (Con), NPs, AE, AE@ZIF-8, and AE-NPs at different time points, AE normalized to 8 mg kg^{-1}. C) Quantitative analysis of tumor fluorescence. Data are presented as mean ± SD, 8 to 10 mice per group, $^{*}P < 0.05$, $^{**}P < 0.01$,$^{***}P < 0.001$ (one-way ANOVA and Bonferroni's multiple comparisons test). D) Photographs of tumors from different treatments. E) Change curves of tumor weight after different treatments, data are presented as mean ± SD, 8 to 10 mice per group, $^{*}P < 0.05$, $^{**}P < 0.01$,$^{***}P < 0.001$ (one-way ANOVA and Bonferroni's multiple comparisons test). F) H&E staining of tumor tissues after different treatments. G,H) The expression of Ki-67 was detected by IHC staining of tumor tissues after different treatments (scale bar: 100 µm), data in (H) are presented as mean ± SD, $n = 3$ mice, $^{*}P < 0.05$, $^{**}P < 0.01$ (one-way ANOVA and Bonferroni's multiple comparisons test). I) Survival curves of mice after different treatments ($n = 6$ mice); Western blot (J) and quantitative analysis (K) of pyroptosis biomarkers CASP-3, C-CASP3, GSDME, and GSDME-N in tumor tissues from different treatments by mean gray value. Data in (K) are presented as mean ± SD, $n = 3$, $^{*}P < 0.05$, $^{**}P < 0.01$, $^{***}P < 0.001$ (one-way ANOVA and Bonferroni's multiple comparisons test).

molecular level, we measured the pyroptosis key biomarkers CASP3, C-CASP3, GSDME, and GSDME-N in tumor tissues from different treatments by western blotting. Compared with the other three groups, AE-NPs significantly enhanced the activation of CASP3 and GSDME (Figure 6J,K). At the same time, AE@ZIF-8 displayed pyroptosis activation ability, this might be induced by AE@ZIF-8 enrichment in tumor tissue.

2.7. AE-NPs Regulated GBM Immune Microenvironment

The above experiments confirmed that AE-NPs activated CASP3/GSDME pyroptosis pathway in vitro and in vivo. As an immunogenic death model, pyroptosis has the potential to activate intrinsic and adaptive immunity to amplify antitumor effect. Therefore, immune cells $CD8^+$ T cells, $CD4^+$ T cells, Treg cells ($FoxP3^+$), macrophage, and their M1 subtype (anti-inflammatory and antitumor subtype, $CD86^+$) were examined by flow cytometry (FCM) and immunofluorescence. $CD8^+$ T cell is critical immune cells in antitumor immunity. Therefore, flow cytometry was performed to identify the infiltration level of $CD8^+$ T cells in tumor tissues from different treatment. The results showed that compare with con group, CD8 expression levels were improved in AE, AE@ZIF-8, and AE-NPS group, especially in the AE-NPs group (the ratio of $CD8^+$ T cells to $CD3^+$ T cells is increased from 31% to 64%) (**Figure 7**A,E). Immunofluorescence also showed pronounced $CD8^+$ T cells expression (Figure S13A, Supporting Information). Since $CD8^+$ T cells are main immune cells that perform tumor killing in vivo, their elevated expression suggest enhanced immune killing effect, but at the same time, the expression of PD-1 was elevated (Figure S13A, Supporting Information). The traditional view is that PD-1 expressed on $CD8^+$ T cell act as an inhibitory receptor mediates immune tolerance, but it was also reported that PD-1 expressed during the early stage of $CD8^+$ T cell activation after antigen stimulation. Thus, the elevated PD-1 may come from $CD8^+$ T cell activation,[34,35] but the exact role needs to be further explored. $CD4^+$ T is an important immune cell, $CD4^+$ T cells and their subtype Treg cells ($FoxP3^+$, mediated immune tolerance) are also detect. Even immunofluorescence showed no significant differences in each group (Figure S13B, Supporting Information), the FCM showed that compare with con group, the $CD4^+$ T increased from 71.45% to 86.18% in AE-NPs group, and with no significant difference in Treg cells (Figure 7B,E,F). The function of tumor-associated macrophages is complex, but M1 subtype (M1Φ) infiltration are conducive to their antitumor effects.[36] FCM showed the ratio of $F4/80^+$ $CD86^+$ cells to $F4/80^+$ cell is increased from 54% in Con group to 71% in AE-NPs group (Figure 7C,G). Immunofluorescence also showed more obvious $Iba1^+$ and CD 86^+ cell expression in tumor of AE-NPs group (Figure S13C, Supporting Information), that suggests more macrophage infiltration and M1 subtype expression. Furthermore antitumor immunity relate cytokines IFN-γ, HMGB1, TNF-α are also measured by qPCR, as shown in Figure 7HJ, compare with control group, the expression of IFN-γ, HMGB1, TNF-α mRNA are increased 6–17 fold in AE-NPs group, this verified the activation of the immune microenvironment.

2.8. AE-NPs Relieved AE-Related Hepatotoxicity and Nephrotoxicity

Similar to many chemotherapeutics, hepatotoxic, and nephrotoxic effects of high concentration AE have been previously reported.[28,37] Meanwhile, high concentrations and unmodified ZIF-8 NPs also has noticeable toxic reactions.[16,33] Therefore, it was necessary to evaluate the safety of the newly constructed AE-NPs. Thus, CCK-8 In vivo, body weight, blood biochemical, and histopathological assays on tumor bearing mouse were performed. Despite a noticeable GBM inhibitory effect with the blank NPs in vivo (Figure 6B,E,F), low dosage of zinc nitrate, 2-methylimidazole, ZIF-8, Tf-PEG-PLGA, and blank NPs did not show noticeable cytotoxicity in vitro (**Figure 8**A). As the concentration continues to increase a certain concentration, zinc nitrate (above 40 μg mL^{-1}), ZIF-8 (above 80 μg mL^{-1}), and NPs (above 80 μg mL^{-1}) all affected cell viability (Figure S15, Supporting Information). Blood biochemical analysis showed that the liver injury biomarkers alanine aminotransferase (ALT), aspartate aminotransferase (AST) (Figure 8B,C), and the renal injury biomarker BUN (Figure 8E) were increased in the AE, AE@ZIF-8, and NPs treated groups, while γ-GT (Figure 8D) and CRE (Figure 8F) were unchanged. Surprisingly, no significant changes in ALT, AST, or BUN were observed in AE-NPs-treated mice. Moreover, the histopathology by HE staining showed that focal necrosis was detected in the liver from the AE treated group, but not in the NPs and AE-NPs treated groups (Figure 8G). These results indicated that liver and kidney injury caused by AE and NPs were significantly reduced by AE-NPs. This is likely the result of enhanced tumor targeting, which reduce drug-related off-target toxicity and side effects.[38] Within 4 weeks, mice in control and NPs group had a body weight loss, but not obvious in AE@ZIF-8 and AE-NPs groups (Figure S12, Supporting Information). For health mice, within 4 weeks, NPs did not affect the body weight (Figure S16A, Supporting Information), organ pathology (Figure S16C, Supporting Information). But there is a slight elevation of ALT on NPs group, and there is no statistic difference in AST, γ-GT, Cr, BUN (Figure S16B, Supporting Information). Moreover, no mouse death during the experiment, shown acceptable security.

3. Discussion

BBB permeability, tumor targeting, and drug toxicity are the main hurdles for chemotherapeutic drugs applied in GBM treatment. Using nanocarriers for drug delivery provides an opportunity to overcome these challenges. Herein, AE-NPs were generated and proven superior to AE alone by the following: 1) Improved BBB permeability; 2) Enhanced tumor targeting and antitumor effects; 3) Reduced drug toxicity.

Improving BBB permeability is key in the treatment of intracranial diseases. The BBB refers to the barrier between the blood and brain formed by the capillary endothelium and glial cells, selectively allowing oxygen and nutrients to enter the central nervous system (CNS), while preventing toxins, microorganisms, and most drugs.[39,40] Although GBM may lead to the disruption of the BBB and enhanced permeability and retention effect (EPR), the barrier remains effective against drugs.[41]

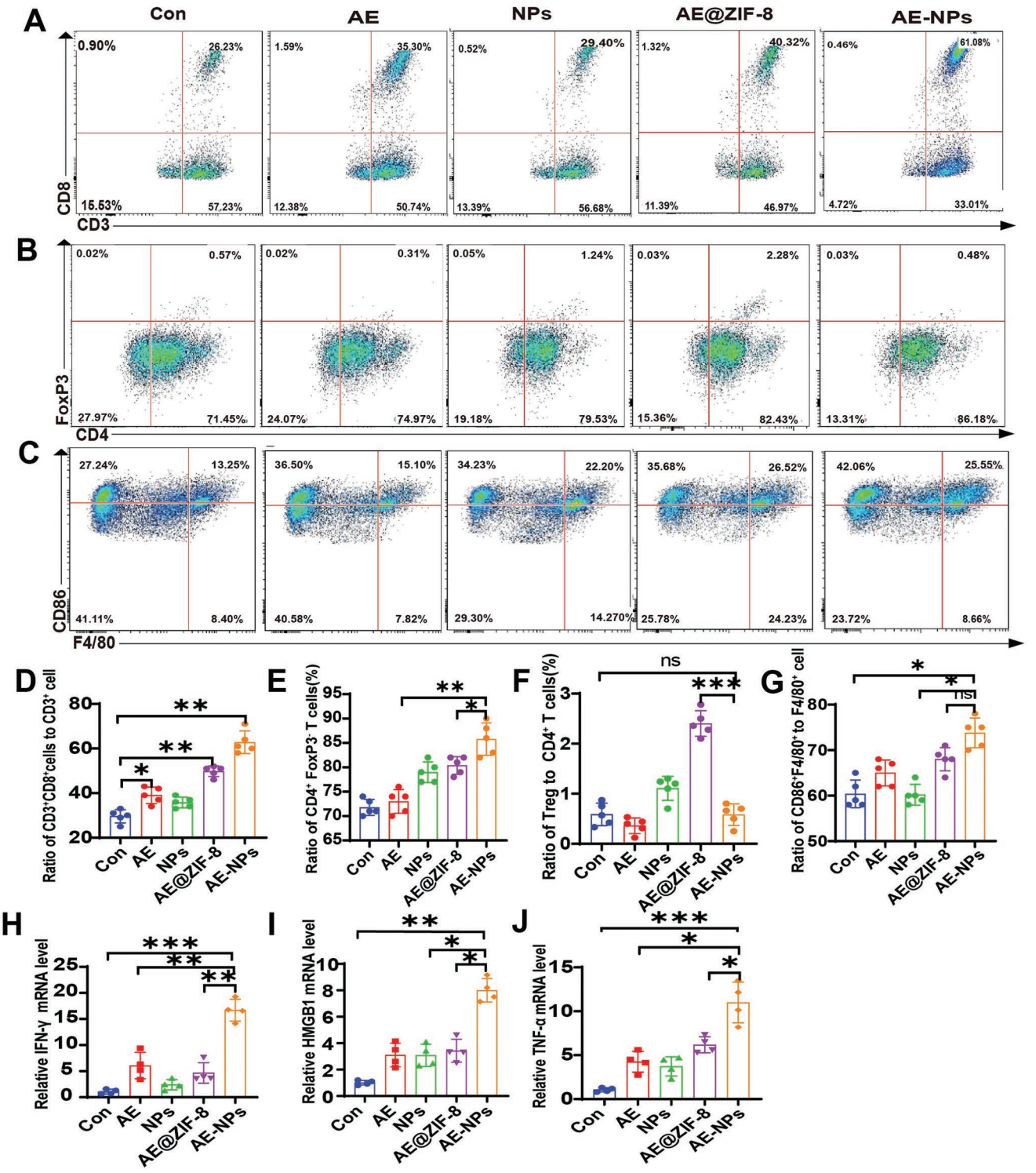

Figure 7. AE-NPs regulate GBM immune microenvironment. Flow cytometry assay of $CD8^+$ T cell (A), CD4+ T and Treg cell (B), macrophage and M1 subtype (C) infiltration in the tumor tissue after different treatments, $n = 5$ mice. D–G) Quantitative analysis of flow cytometry, Data are presented as mean ± SD, $n = 5$ mice, $^*P < 0.05$, $^{**}P < 0.01$,$^{***}P < 0.001$ (one-way ANOVA and Bonferroni's multiple comparisons test). H–J)The expression of IFN-γH), HMGB1 I), TNF-αJ) mRNA in GBM tissue after different treatment, assayed by qPCR. All data are represented as means ± SD ($n = 5$); $^*P < 0.05$, $^{**}P < 0.01$, $^{***}P < 0.001$ compared with the control group (one-way ANOVA and Bonferroni's multiple comparisons test).

As the tumor deteriorates and progresses, the tumor membrane ruptures, and the structure of the BBB and its functions will also be changed,[42,43] eventually leading to 98% of small molecules and almost all macromolecules being insulated from the CNS.[44] These factors lead to the failure of most clinical drugs for the treatment of GBM. Significantly, in this work, our

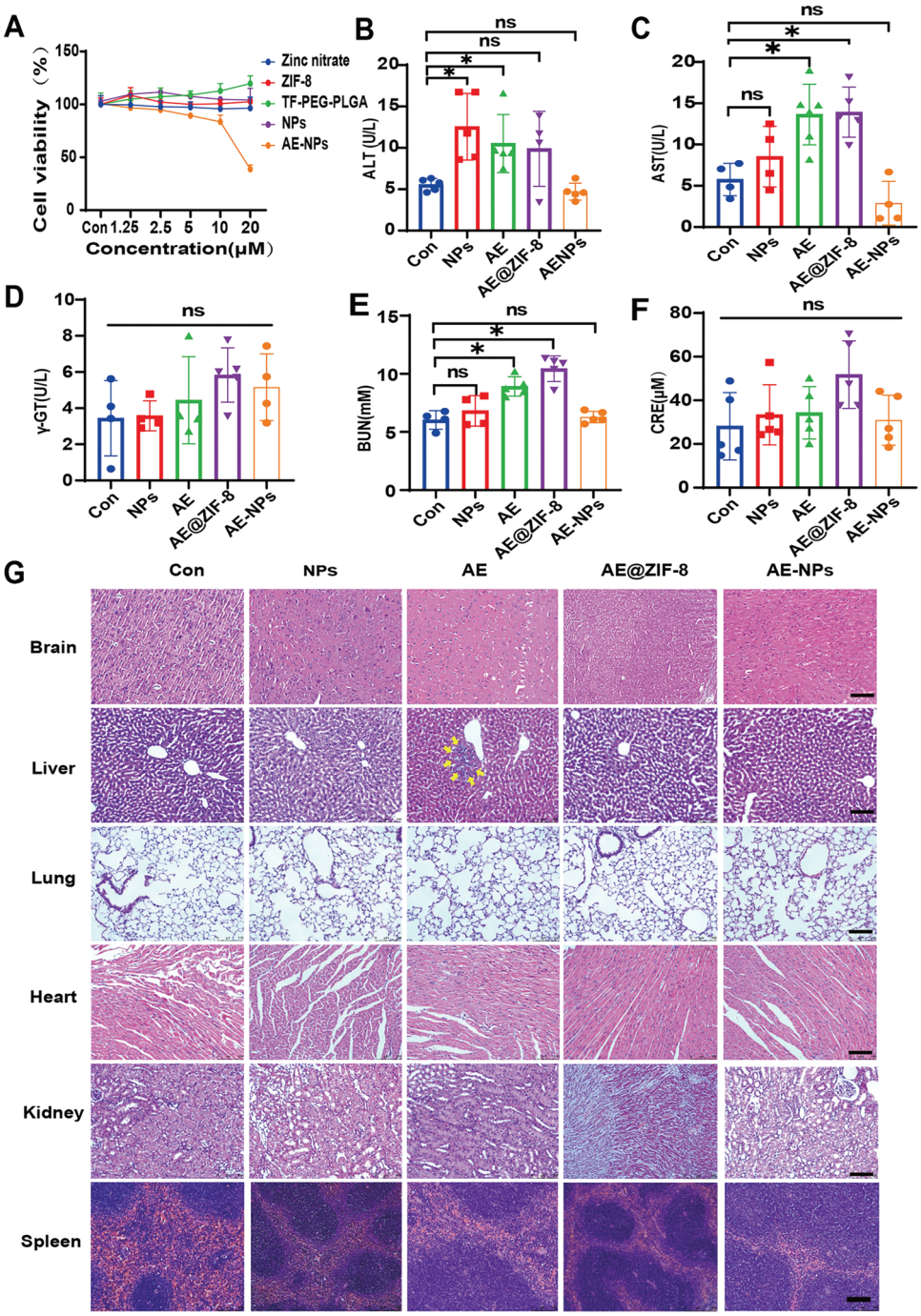

Figure 8. AE-NPs relieved hepatotoxicity and nephrotoxicity. A) Cytotoxicity of zinc nitrate, ZIF-8, Tf-PEG-PLGA, NPs, and AE-NPs on U87MG cells was measured by CCK-8 ($n = 3$); ALT (B), AST (C), γGT (D), CRE (E), and BUN (F) values in mouse serum after different treatments. All values are presented as mean ± SD, 4–6 mice per group, $^{*}P < 0.05$, $^{**}P < 0.01$ (one-way ANOVA and Bonferroni's multiple comparisons test). G) HE staining of the pivotal organs after different treatments. The yellow arrow points to the lesion zone (scale bar: 100 μm).

constructed AE-NPs improved the BBB penetration, which probably because the Tf-PEG-PLGA coating prolonged the blood circulation time and altered BBB penetration mode.

Enhanced tumor targeting is beneficial for antitumor effects and reducing drug-related toxicity and side effects.[38] Constructed AE-NPs achieved tumor targeting and enrichment (Figure 5D,E), likely related to TfR are highly expressed in tumor tissue, hence Tf can anchor the nanoparticles to tumor tissue and improve tumor enrichment. Furthermore, the ability of ZIF-8 NPs responded degradation in acidic tumor microenvironment also has a synergistic effect to improve the tumor targeting effect.[16]

In this study, we found that AE acts as a pyroptosis inducer. Additionally, we observed that AE at a concentration of IC50

(48.7 μM, U87MG) significantly inhibited the activity of U87 cells after 48 h (Figure 1B). However, there was no significant activation of CASP3 and GSDME (Figure 2D), suggesting that AE-induced pyroptosis may not be the only mechanism underlying its anti-GBM effects. Moreover, we found that AE-induced pyroptosis in U87MG cells is concentration-dependent, with high doses inducing GBM pyroptosis but not low doses (Figure 2D).

Our research also shows that tumor-targeted delivery of AE-NPs enhances AE enrichment in GBM (Figure 5D,E). This concentration difference makes the induction of tumor tissue pyroptosis feasible (Figure 6J), while minimizing pyroptosis in normal brain tissue, which is considered one of the reasons for the side effects of chemotherapy drugs.[27] This advantage supports our decision to choose AE as a pyroptosis-inducing agent.

The materials used in this study have been shown to be safe in previous studies, but high concentrations and unmodified ZIF-8 NPs can have noticeable toxic reactions.[16,33] These are mainly derived from the rapid degradation of ZIF-8 NPs.[33] It was reported that unmodified ZIF-8 NPs could kill not only cells but also animals, however, such toxic reactions can be alleviated by appropriate modification.[33] We utilized ZIF-8 NPs as drug carriers in this study, and the coating of Tf-PEG-PLGA polymer did not show increased cytotoxicity on GBM cells (Figure 8A). Although ALT, AST, and BUN levels were elevated by NPs, the organ toxicity of AE-NPs was not obvious (Figure 8B,C,E). At the same time, the NPs showed an obvious inhibitory effect and necrosis-promoting effect on GBM cells (Figure 6F), meanwhile no pathological damage to the brain and vital organs was observed (Figure 8G). These results suggest that Tf-PEG-PLGA coated ZIF-8 NPs suppress GBM without obvious toxic side effects, which likely attributed to the modification of Tf-PEG-PLGA anchoring ZIF-8 NPs in tumor tissue. The acidic microenvironment promotes ZIF-8 NPs degradation, and the cytotoxic effect is restricted to tumor tissue.

Immunosuppressive tumor microenvironment, which suppress immune responses and support tumor growth is one of the biggest hurdles to effective therapy for GBM.[45] Pyroptosis of the GSDME pathway has good prospects in antitumor therapy because it can mediate both cell death and antitumor immune activation. Couple with pyroptosis, intracellular antigens (such HMGB1, IL-1β) released, promote DC maturation, initiate T-cell clone, enhance tumor killing effect, pyroptosis is considered as a new tumor immunotherapy.[46] At present, there are limited reports on anti-GBM by promote pyroptosis. Herein, the targeted delivery of AE by NPs to GBM enhanced AE-mediated GBM pyroptosis in vivo (Figure 6J,K). Furthermore, AE-NPs also enhanced $CD8^+$ T cells, $CD4^+$ T cells, macrophage M1 subtype GBM infiltration, and increased the expression of IFN-, HMGB1, TNF-αin mRNA level (Figure 7). Therefore, our research may offer a new strategies for GBM immunotherapy.

Despite the big advantages of Aloe-emodin for cancer therapy, the hepatotoxicity and nephrotoxicity brought by high concentration of AE are also main problems for its clinical application. It was reported that these defects were mainly caused by high concentration of AE induced FAS death, mitochondrial damage, endoplasmic reticulum stress provoking, and DNA damage.[37,47,48] Our study showed that AE significantly inhibited GBM cells and GBM growth both in vitro and in vivo (Figures 1B,6B–E; and Figure S1, Supporting Information), but it was accompanied by elevated liver and kidney injury serologic markers (ALT, AST, BUN) and histopathological injury of the liver (Figure 8B,C,G). These observations are consistent with previous reports of hepatotoxicity and nephrotoxicity. However, when AE was encapsulated by NPs, there were no significant differences in blood biochemical changes (Figure 8B,C,E) or histopathological (Figure 8G) injury compared to control groups, indicating that NPs encapsulation effectively alleviated AE-related hepatotoxicity and nephrotoxicity. This may be attributed to enhanced tumor targeting, but the in-depth mechanism needs further exploration.

4. Conclusion

In summary, AE was proved as a pyroptosis booster to suppress GBM through the CASP3/GSDME pathway both in vitro and in vivo. By loaded with a pH responsive and BBB penetrating nanocarrier, improved BBB penetration, tumor targeting, enhanced antitumor efficacy, and reduced toxicity effect were realized. In addition, AE-NPs have also been proved to enhance $CD8^+$ T, $CD4^+$T, macrophage M1 subtype GBM infiltration, prolong the survival rate of tumor-bearing mice. Overall, our study provides a new strategy for the treatment of GBM and provides a BBB-penetrating, tumor-targeting, high-efficiency, and attenuated drug carrier for intracranial tumor therapy.

5. Experimental Section

Main Materials: Aloe-emodin (AE, 99%, Chengdu Alpha). Zinc nitrate hexahydrate ($Zn(NO_3)_2{\cdot}6H_2O$, 99.998%, Aladdin), *N*-hydroxy succinimide (NHS, 98%, Aladdin), *N*-(3-Dimethylaminopropyl)-*N′*-ethylcarbodiimide hydrochloride (EDC·HCl, 98%, Aladdin), 2-methylimidazole ($C_4H_6N_2$, 98%, Aladdin), transferrin (95%, Aladdin). Indocyanine green (ICG, 75%, Macklin), PLGA20k-PEG5k-COOH was purchased from Xi"an Ruixi Biological Technology Co. Ltd. (Xi"an, China). Recombinant anticleaved caspase-3 antibody, recombinant anti-DFNA5/GSDME N-terminal antibody, anti-Iba1 antibody, Anti-CD4 antibody (EPR19514), PD-1 antibody, and anti-Ki67 antibody were purchased from Abcam Plc Co., Ltd. (Cambridge, UK). CD86(B7-2(D-6)) antibody, CD8-α (D-9) were obtained from SantaCruz (Dallas, USA), PE antimouse CD8a were purchased from Biolegend (CA, USA). PE Rat Anti-Mouse F4/80(T45-2342), PE-Cy7 Rat Anti-Mouse CD86(GL1), APC-Cy7 Rat Anti-Mouse CD45(30-F11), PE-Cy7 Hamster Anti-Mouse CD3e(145-2C11), APC Rat Anti-Mouse CD4(RM4-5), PE Rat anti-Mouse Foxp3(R16-715), were purchased from BD Pharmingen (NJ, USA). FoxP3 Monoclonal Antibody were purchased from eBioscience (CA, USA), Donkey anti-Goat IgG-AlexaFluor 488, Donkey anti-Rabbit IgG-Alexa Fluor 594 (Shanghai, China), β-Tubulin rabbit monoclonal antibody, FITC-labeled goat anti-rabbit IgG, horseradish peroxidase-labeled goat anti-rabbit IgG (H+L), and LDH Release Assay Kit were purchased from Beyotime Biotechnology Co., Ltd. (Shanghai, China). And alanine aminotransferase (ALT) assay kit, creatinine (CRE) assay kit, aspartate aminotransferase (AST) assay kit, blood urea nitrogen (BUN) assay kit, γ-glutamyl transferase (γ-GT) assay kit were purchased from Nanjing Jiancheng Bioengineering Research Institute Co., Ltd. (Nanjing, China).

Synthesis of AE@ZIF-8 NPs: AE-loaded ZIF-8 NPs (AE@ZIF-8 NPs) were prepared by a self-assembly method.[19,49] First, 75 mg of zinc nitrate was added to 2.5 mL of methanol and sonicated to dissolve with a 120 W ultrasonic bath for 2 min (solution A). Meanwhile, 165 mg of 2-methylimidazole and aloe-emodin (0, 2, 6, 10, 20 mg) were dissolved in

5 mL of methanol and sonicated with a 120 W ultrasonic bath for 5 min (solution B). Subsequently, solution B was stirred for 5 min at 250 rpm under room temperature. Next, solution A was dropped into solution B under 250 rpm stirring condition. After that, the mixture was continue stirred in the dark at room temperature for 1 h, and then kept for another 1 h at 4 °C. Finally, the mixture was centrifuged at 12 000 rpm for 10 min, washed with methanol three times to obtain AE@ZIF-8 nanoparticles, and resuspended in 5 mL methanol or normal saline (NS) containing 1% poloxamer (F127) (1% F127 NS) for further experiments.

Preparation of Tf-PEG-PLGA: Tf was conjugated to PEG-PLGA by a two-step EDC/NHS coupling method.[50] With the catalysis of EDC/NHS, the —COOH of COOH-PEG-PLGA interacts with $-NH_2$ from Tf to generate amide bonds, thereby obtaining Tf-modified PEG-PLGA (Tf-PEG-PLGA) (Scheme 1A). Briefly, 10 mg COOH-PEG-PLGA was dissolved in 4.5 mL methanol in a 120 W ultrasonic bath for 5 min, then 250 µL of EDC·HCl (1 mg mL^{-1}) and 250 µL of NHS (1 mg mL^{-1}) were added and magnetically stirred at room temperature for 4 h at 250 rpm. Then, 200 µL of transferrin aqueous solution (1 mg mL^{-1}) was added dropwise, stirred in the dark for 2 h, and incubated for overnight at 4 °C.

Preparation of AE-NPs: The above AE@ZIF-8 NPs methanol solution was mixed with Tf-PEG-PLGA methanol solution in volume ratios of 5:5, 6:4, 7:3, 8:2, and 9:1 at room temperature with magnetic stirring at 250 rpm for 4 h in the dark. The samples were centrifuged at 12 000 rpm for 10 min, and the precipitate was taken to obtain the final AE-NPs product, which was washed twice with methanol. Then, the NPs were resuspended in 75% ethanol, soaked for 30 min to remove bacteria, and washed twice with 1% F127 NS.

Characterizations of ZIF-8 NPs, AE@ZIF-8 NPs, and AE-NPs: Dynamic light scattering (DLS) and transmission electron microscopy (TEM) were used to detect the size of nanoparticles. For detection nanoparticle size and zeta potential, the NPs were distributed in methanol, 1% F127NS, and 1% F127NS+10% FBS, respectively, and analyzed by a Malvern laser particle size analyzer (DTS1070, Malvern, UK). The stability of nanoparticles was evaluated by hydrodynamic particle size at 0, 12, 24, 48, 72, and 96 h. The structure and morphology of blank ZIF-8 NPs, AE@ZIF-8 NPs, and AE-NPs were observed by TEM (HITACHI, Japan) with an accelerating voltage of 80 kV. TEM samples were tweezers held on carbon-coated copper grids (200 mesh; Ted Pella, Inc., USA), immersed in a particle solution, removed, and air-dried prior to imaging. The size from TEM was analyzed with ImageJ software. Each picture was marked with 100 nanoparticles, three pictures were recorded, and the detection results were imported to Origin 2021 software to obtain the size. Furthermore, the successful encapsulation of AE and ICG into Tf-PLGA-PEG coated ZIF-8 NPs was detected through remarkable absorption at 255 and 780 nm by UV–vis absorption spectroscopy (Puxi General Instrument Co., Ltd. China). The coating of Tf-PEG-PLGA on ZIF-8 NPs was confirmed by FTIR spectra and TEM images.

Drug Loading Degree and Efficiency Detection: The content of AE was detected by UV–vis absorption at 255 nm. A 200 µL sample was dropped into a cuvette containing 2.8 mL methanol solution with a pH of 1.5. According to the standard curve, the content of AE in the sample was calculated. AE loading degree (LD, %) = amount of encapsulated AE/weight of nanoparticles; AE encapsulation rate (%) = amount of encapsulated AE/total input amount of AE. the connection efficiency of transferrin was calculated by a BCA kit, Tf loading efficiency (LE, %) = weight of transferrin in nanoparticles/total input amount of transferrin.

In Vitro Release and pH-Responsive Analysis: AE-NPs were dispersed into 1.0 mL of 1% F127 NS (pH = 7.4; pH = 5.5) and shaken at 37 °C gently in dark. The solution was first centrifuged at 12 000 rpm for 10 min, and then 900 µL of supernatant was withdrawn and analyzed by a UV spectrophotometer at 255 nm at indicated time points. Then, 900 µL of fresh medium was added and sonicated until dispersed well. Calculate cumulative release rates at selected time intervals. The alternative sample disposal method is as above. At selected time intervals, the appearance of AE-NPs from different pH values was observed by TEM, and size was test by Malvern laser particle size analyzer.

Cells and Animals: U87MG, DBTRG, U251, HeLa, HepG2, A549, HMO6, BV2 cells were purchased from ATCC (American Type Culture Collection) and stored in the laboratory and cultured in DMEM containing 10% FBS, 1% penicillin–streptomycin solution, 2 mM l-glutamine, and maintained at 37 °C with 5% CO_2 humidity. GL261-Luc was purchased from Shanghai Yansheng Industrial Co., Ltd (Shanghai, China), and used as the transplanted tumor model. GL261-Luc cells were stored as recommended by ATCC, cultured and cryopreserved according to the manufacturer's protocol. C57BL/6J mice were purchased from Laboratory Animal Center of Hubei University of Medicine (Hubei, China) and bred according to the Guide for the Care and Use of Laboratory Animals of the National Institutes of Health. The experimental protocol of this study was reviewed and approved by the Laboratory Animal Welfare Ethics Review Committee of Hubei University of Medicine (Hubei University of Medicine Animal (welfare) No. 2022-Experiment 015).

Cell Viability Assay: CCK-8 was used to detect the cell viability. U87MG and GL261 cells were seeded in 96-well plates at a density of 4000 cells per well. Twelve hours later, cell culture medium containing gradient concentrations of AE was administered and cocultured, 0.1% DMSO was used as the control (Con), and 10 µL of CCK-8 solution was added to each well at 24, 48, and 72 h and incubated in an incubator (37 °C, 5% CO_2) for 2 h. The absorbance at 450 nm was measured using a SpectraMax 190 microplate reader (Molecular Devices, USA).

Screening of AE-Related Targets: Swiss Target Prediction database was used to query AE targets and related target genes. Then, the Pharm Mapper database was applied to restrict the species to human, and the Target Net database was used to identify potential target genes. After merging the targets of each database, the duplicate data were deleted, and the aloe-emodin-related targets were uniformly transformed using the UniPort protein standardization database.

Collection of Targets of GBM: Using "Glioblastoma" as the keyword, the related targets were screened by the OMIM database, Gene Cards database, and TTD database. Targets were selected according to the principle of a Gene Cards database relevance score > 5, and the published literature was found to supplement the unscreened targets. After merging three disease database targets, the repeat values were deleted to obtain the final target for interaction with glioblastoma.

Construction of the AE-GBM Target Protein–Protein Interaction (PPI) Network: After merging and compiling the search results from the database, duplicate targets were removed. The intersection between the predicted targets of AE active ingredients and the retrieval results of glioblastoma-related target genes was determined, and the common targets were screened as possible targets of AE in GBM. The Venny 2.1.0 to map GBM-related targets and active ingredient targets in the form of Venn diagrams was applied. The intersection targets were uploaded to the STRING database (version 11.5) to construct the PPI network, and the key targets were subsequently screened and analyzed subsequently, the scoring condition was set to >0.40, and the selected target proteins were limited to "Homo sapiens." Then, the key protein targets were visually analyzed by Cytoscape3.7.2 software. The function of the plug-in "Analysis Network" was used for analysis, and the key targets were sorted by "Degree." In the PPI network, the edges represent protein–protein associations, more lines suggesting greater correlation.[51] Databases and software used in the network pharmacology analysis were list at Table S1 (Supporting Information).

LDH Release: LDH release was detected by an LDH Release Assay Kit. U87 cells were first seeded into 96-well plate at the density of 5000 cells per well and incubated for 24 h. After that, a gradient concentration of AE was added into the cells and coincubated for 48 h. The supernatant from each well was collected into a new 96-well plate to detect the level of LDH release by the LDH Release Assay Kit, and the absorbance at 490 nm of the supernatant was detected by a SpectraMax 190 microplate reader (Molecular Devices, USA).

qPCR Assay: Total RNA was extracted from AE treated U87MG, GL261 cells and tumor tissue after different treatment by Trizol, using an ABScript II Reverse Transcriptase kit (RK21400, ABclonal, China) to reverse-transcribe and synthesize cDNA. The obtained cDNA was used as a template for subsequent qPCR experiments. Primer sequences used in this work were listed in Table S2 (Supporting Information).

Confocal High-Content Imaging: U87MG cells were seeded into 24-well plates, 3000 cells per well. Then, the cells were treated with AE and AE-NPS, the AE concentrations were equilibrated to 50 μM, 0.2% DMSO was used as a control, and the Operetta CLS confocal high-content imaging analysis system (Perkin Elmer, USA) was used for detection. There were 8 detection views in each well, taking pictures once per hour (200X), and observing for 72 h.

Body Distribution: ICG-NPs were prepared as nanotrackers, and the distribution of NPs in vivo was analyzed by optical live imaging and cryosections. C57BL/6J mice were treated with ICG and ICG-NPs through the tail vein, and the dosage of ICG was normalized to 3 mg kg^{-1}. At selected time intervals, the mice were anesthetized and sacrificed. The fluorescence expression of the brain and vital organs was examined under a fluorescence imaging system (Calliper, USA). For cryosections, tumor-bearing mice were administered and treated in the same way as above, brain (with tumor) were taken for cryosections (10 μm), the nuclei were stained with DAPI after fixation, and the drug distribution was observed under a fluorescence microscope (Leica DMI6000B, Leica, Germany). The distribution of AE in brain and tumor was detected by liquid chromatography-mass spectrometry (LC-MS): Tumor bearing mice were injected with AE, AE@ZIF-8, and AE-NPs (the amount of AE was balanced to 8 mg kg^{-1}) through tail vein, and the tumor bearing brain tissue was obtained in 2 h, then brain and tumor were separated and weighed, Homogenized in normal saline, 1, 8-dihydroxy-anthraquinone was used as the internal standard, methanol was added, and all supernatants were dried with nitrogen. The precipitation was redissolved with the initial mobile phase (10% methanol +90% 2 mM ammonium acetate), vortexed for 5 min, centrifuged, and 5 μL supernatant was taken for detection. Calibration standards and quality control (QC) samples were prepared and extracted same as the samples. The analysis was performed using a Waters ACQUITY UPLC system (Waters, Milford, MA) and a Micromass Quattro Micro API mass spectrometer (Waters, Milford, MA).Chromatographic separation was performed on an ACQUITY UPLC BEH C18 Column (2.1 × 100 mm; 1.7 μm), maintained at 45 °C. The flow rate was maintained at 300 μL min^{-1}. The initial flow conditions were 90% solvent A (2 mM ammonium acetate) and 10% solvent B (methanol). The gradient elution program was as follows: 0–0.5 min, 10% B; 0.5–1.2 min, 10–35% B;1.2–3.5 min, 35–70% B; 3.5–4.2 min, 70–90% B;4.2–5.2 min, 90% B; 5.2–5.5 min, 90–10% B; and 5.5–6.0 min, 10% B. The mass spectrometer was operated under multiple reaction monitoring (MRM) mode with negative electrospray ionization. Mass spectrometer was operated using the following parameters: Electrospray ion source, gas temperature, 400 °C; gas flow, 800 L h^{-1}; capillary 3 Kv.

Blood Biochemical Examination: Blood was collected by cardiac puncture after anesthesia at the end of the treatment, and serum was collected by centrifugation. ALT, AST, Cr, γ-GT, and BUN assay kits were used to assay ALT, AST, Cr, γ-GT, and BUN.

HE Staining and Immunohistochemistry: Paraffin sections from tumor tissue and vital organs (brain, heart, spleen, liver, lung, and kidney) were dewaxed, rehydrated, and antigen repaired. The paraffin sections were stained with eosin and hematoxylin for HE. For IHC staining, the paraffin sections were incubated in 3% hydrogen peroxide for 12 min at room temperature. And then blocked with 5% BSA for 40 min, stained with 1:200 anti-Ki67 antibody (ab15580, Abcam, USA) overnight at 4 °C, and secondary antibody were incubated for 1 h at 37 °C, Diaminobenzidine was applied for coloration for 3 min at room temperature, the nucleus was stained by hematoxylin.

Flow Cytometry: The tumors were harvested from the GBM-bearing mice after different treatment. Then homogenized in DMEM containing collagenase IV at 37 °C. The tumor-infiltrating immune cells were collected by centrifugation (3000 rpm,15 min), and resuspended in PBS containing 2% FBS and nonspecific antibody binding was blocked with CD16/CD32. After strain with FIXABLE VIABILITY DYE EF506. $CD8^+$T cells were labeled with CD45, CD3, and CD8 antibodies, $CD4^+$T cells were labeled with CD45, CD3, and CD4 antibodies, and Treg cells were further labeled with FoxP3 antibody base on $CD4^+$ T cells. M1Φ was labeled with CD45, F4/80, and CD86 antibodies, FoxP3 were stained using a Transcription Factor Buffer Set. Gating strategy for flow cytometry were showed in Figure S14 (Supporting Information).The cells were measured with a flow cytometer (Sony 3800, Japan) and analyzed using SA3800 Software Version 2.0.4.14073.

Statistical Analysis: All experiments were repeated at least three independent times, and data were expressed as the mean ± SD. Statistical analysis was performed using a 2-tailed Student's *t*-test or one-way ANOVA and Bonferroni's multiple comparisons test when multiple groups were evaluated. P values < 0.05 were considered significant differences.

Supporting Information

Supporting Information is available from the Wiley Online Library or from the author.

Acknowledgements

X.F., Z.C., and W.Z. contributed equally to this work. This work was supported by the National Natural Science Foundation of China (Nos. 81671831, 82073232, 81700769, and 81641028), Guiding project of Scientific Research Plan of Education Department of Hubei Province (No. B2022131), Hubei health commission youth talents project (No. WJ2021F023), the Hubei Science & Technology Department Foundation (Nos. 2020CFB558 and 2018ACA162), the Key Projects of Hubei Education (No. D20202103), the Department of Biomedical Research Foundation, Hubei University of Medicine (No. HBMUPI201803), the Advantages Discipline Group (medicine) Project in Higher Education of Hubei Province (Nos. 2022XKQT3 and 2022XKQY1), and the Scientific Research Project of Shiyan Science and Technology Bureau (Nos. 21Y06 and 21Y38).

Conflict of Interest

The authors declare no conflict of interest.

Data Availability Statement

The data that support the findings of this study are available from the corresponding author upon reasonable request.

Keywords

aloe-emodin, blood–brain barrier, glioblastoma, pyroptosis, tumor target

Received: December 5, 2022
Revised: April 1, 2023
Published online: April 17, 2023

[1] M. L. Goodenberger, R. B. Jenkins, *Cancer Genet.* **2012**, *205*, 613.
[2] M. Carlberg, L. Hardell, *Biomed Res. Int.* **2017**, *2017*, 9218486.
[3] L. P. Ganipineni, F. Danhier, V. Préat, *J. Controlled Release* **2018**, *281*, 42.
[4] A. F. Hottinger, R. Stupp, K. Homicsko, *Chin. J. Cancer* **2014**, *33*, 32.
[5] D. H. Upton, C. Ung, S. M. George, M. Tsoli, M. Kavallaris, D. S. Ziegler, *Theranostics* **2022**, *12*, 4734.
[6] Z. Chen, D. Hambardzumyan, *Front. Immunol.* **2018**, *9*, 1004.
[7] P. Broz, V. M. Dixit, *Nat. Rev. Immunol.* **2016**, *16*, 407.

[8] Z. Zhang, Y. Zhou, S. Zhao, L. Ding, B. Chen, Y. Chen, *Adv. Sci.* **2022**, *9*, 2203583.
[9] Z. Li, F. Mo, Y. Wang, W. Li, Y. Chen, J. Liu, T. J. Chen-Mayfield, Q. Hu, *Nat. Commun.* **2022**, *13*, 6321.
[10] P. Yu, X. Zhang, N. Liu, L. Tang, C. Peng, X. Chen, *Signal Transduct. Target Ther.* **2021**, *6*, 128.
[11] Y. Tan, Q. Chen, X. Li, Z. Zeng, W. Xiong, G. Li, X. Li, J. Yang, B. Xiang, M. Yi, *J. Exp. Clin. Cancer Res.* **2021**, *40*, 153.
[12] Y. Fang, S. Tian, Y. Pan, W. Li, Q. Wang, Y. Tang, T. Yu, X. Wu, Y. Shi, P. Ma, Y. Shu, *Biomed. Pharmacother.* **2020**, *121*, 109595.
[13] C. Giuliani, B. Altieri, C. Bombelli, L. Galantini, G. Mancini, A. Stringaro, *Langmuir* **2015**, *31*, 76.
[14] H. Z. Lee, C. J. Lin, W. H. Yang, W. C. Leung, S. P. Chang, *Cancer Lett.* **2006**, *239*, 55.
[15] X. Li, J. Tsibouklis, T. Weng, B. Zhang, G. Yin, G. Feng, Y. Cui, I. N. Savina, L. I. Mikhalovska, S. R. Sandeman, C. A. Howel, S. V. Mikhalovsky, *J. Drug Target* **2017**, *25*, 17.
[16] J. Yan, C. Liu, Q. Wu, J. Zhou, X. Xu, L. Zhang, D. Wang, F. Yang, H. Zhang, *Anal. Chem.* **2020**, *92*, 11453.
[17] C. Wang, R. Zhang, X. Wei, M. Lv, Z. Jiang, *Adv. Immunol.* **2020**, *145*, 187.
[18] N. Katila, R. Duwa, S. Bhurtel, S. Khanal, S. Maharjan, J. H. Jeong, S. Lee, D. Y. Choi, S. Yook, *J. Controlled Release* **2022**, *346*, 1.
[19] D. R. Owens, N. A. Peppas, *Int. J. Pharm.* **2006**, *307*, 93.
[20] S. M. Jusu, J. D. Obayemi, A. A. Salifu, C. C. Nwazojie, V. Uzonwanne, O. S. Odusanya, W. O. Soboyejo, *Sci. Rep.* **2020**, *10*, 14188.
[21] P. Rafiei, A. Haddadi, *Int. J. Nanomed.* **2017**, *12*, 935.
[22] K. B. Johnsen, A. Burkhart, L. B. Thomsen, T. L. Andresen, T. Moos, *Prog. Neurobiol.* **2019**, *181*, 101665.
[23] E. Ryschich, G. Huszty, H. P. Knaebel, M. Hartel, M. W. Büchler, J. Schmidt, *Eur. J. Cancer* **2004**, *40*, 1418.
[24] N. özenver, M. Saeed, L. Ö. Demirezer, T. Efferth, *OncoTargets Ther.* **2018**, *9*, 17770.
[25] Y. Xiao, T. Zhang, X. Ma, Q. C. Yang, L. L. Yang, S. C. Yang, M. Liang, Z. Xu, Z. J. Sun, *Adv. Sci.* **2021**, *8*, 2101840.
[26] J. Ding, K. Wang, W. Liu, Y. She, Q. Sun, J. Shi, H. Sun, D. C. Wang, F. Shao, *Nature* **2016**, *535*, 111.
[27] Y. Wang, W. Gao, X. Shi, J. Ding, W. Liu, H. He, K. Wang, F. Shao, *Nature* **2017**, *547*, 99.
[28] X. Dong, Y. Zeng, Y. Liu, L. You, X. Yin, J. Fu, J. Ni, *Phytother. Res.* **2020**, *34*, 270.
[29] R. Chen, J. Zhang, Y. Hu, S. Wang, M. Chen, Y. Wang, *Am. J. Chin. Med.* **2014**, *42*, 275.
[30] R. G. Thorne, C. Nicholson, *Proc. Natl. Acad. Sci. USA* **2006**, *103*, 5567.
[31] S. K. Hobbs, W. L. Monsky, F. Yuan, W. G. Roberts, L. Griffith, V. P. Torchilin, R. K. Jain, *Proc. Natl. Acad. Sci. USA* **1998**, *95*, 4607.
[32] H. Zheng, Y. Zhang, L. Liu, W. Wan, P. Guo, A. M. Nyström, X. Zou, *J. Am. Chem. Soc.* **2016**, *138*, 962.
[33] L. Su, Q. Wu, L. Tan, Z. Huang, C. Fu, X. Ren, N. Xia, Z. Chen, X. Ma, X. Lan, Q. Zhang, X. Meng, *ACS Appl. Mater. Interfaces* **2019**, *11*, 10520.
[34] D. Sugiura, T. Maruhashi, I. M. Okazaki, K. Shimizu, T. K. Maeda, T. Takemoto, T. Okazaki, *Science* **2019**, *364*, 558.
[35] E. Ahn, K. Araki, M. Hashimoto, W. Li, J. L. Riley, J. Cheung, A. H. Sharpe, G. J. Freeman, B. A. Irving, R. Ahmed, *Proc. Natl. Acad. Sci. USA* **2018**, *115*, 4749.
[36] Z. Zheng, J. Zhang, J. Jiang, Y. He, W. Zhang, X. Mo, X. Kang, Q. Xu, B. Wang, Y. Huang, *J. Immunother. Cancer* **2020**, *8*, 1.
[37] F. Nesslany, S. Simar-Meintières, H. Ficheux, D. Marzin, *Mutat. Res.-Fundam. Mol. Mech. Mutagen.* **2009**, *678*, 13.
[38] K. Bouzinab, H. S. Summers, M. Stevens, C. J. Moody, N. R. Thomas, P. Gershkovich, N. Weston, M. B. Ashford, T. D. Bradshaw, L. Turyanska, *ACS Appl. Mater. Interfaces* **2020**, *12*, 12609.
[39] N. J. Abbott, A. A. Patabendige, D. E. Dolman, S. R. Yusof, D. J. Begley, *Neurobiol. Dis.* **2010**, *37*, 13.
[40] H. K. Kimelberg, M. Nedergaard, *Neurotherapeutics* **2010**, *7*, 338.
[41] R. K. Oberoi, K. E. Parrish, T. T. Sio, R. K. Mittapalli, W. F. Elmquist, J. N. Sarkaria, *Neuro Oncol.* **2016**, *18*, 27.
[42] N. S. Ningaraj, M. Rao, K. Hashizume, K. Asotra, K. L. Black, *J. Pharmacol. Exp. Ther.* **2002**, *301*, 838.
[43] C. Zhan, W. Lu, *Curr. Pharm. Biotechnol.* **2012**, *13*, 2380.
[44] C. A. René, R. J. Parks, *Pharmaceutics* **2021**, *13*, 492.
[45] H. J. Kim, J. H. Park, H. C. Kim, C. W. Kim, I. Kang, H. K. Lee, *Nat. Commun.* **2022**, *13*, 6211.
[46] J. X. Fan, R. H. Deng, H. Wang, X. H. Liu, X. N. Wang, R. Qin, X. Jin, T. R. Lei, D. Zheng, P.-H. Zhou, Y. Sun, X.-Z. Zhang, *Nano Lett.* **2019**, *19*, 8049.
[47] X. Dong, J. Fu, X. Yin, C. Qu, C. Yang, H. He, J. Ni, *Cell. Physiol. Biochem.* **2017**, *42*, 685.
[48] S. Zhu, J. Jin, Y. Wang, Z. Ouyang, C. Xi, J. Li, Y. Qiu, J. Wan, M. Huang, Z. Huang, *Food Chem. Toxicol.* **2012**, *50*, 1149.
[49] Y. Pan, Y. Liu, G. Zeng, L. Zhao, Z. Lai, *Chem. Commun.* **2011**, *47*, 2071.
[50] A. Halder, P. Mukherjee, S. Ghosh, S. Mandal, U. Chatterji, A. Mukherjee, *Mater. Today: Proc.* **2018**, *5*, 9698.
[51] D. Szklarczyk, A. L. Gable, K. C. Nastou, D. Lyon, R. Kirsch, S. Pyysalo, N. T. Doncheva, M. Legeay, T. Fang, P. Bork, L. J. Jensen, C. von Mering, *Nucleic Acids Res.* **2020**, *49*, D605.